

Article

Proton Affinity in the Chemistry of Beta-Octamolybdate: HPLC-ICP-AES, NMR and Structural Studies

Victoria V. Volchek ¹ , Nikolay B. Kompankov ¹, Maxim N. Sokolov ¹  and Pavel A. Abramov ^{1,2,*} 

¹ Nikolaev Institute of Inorganic Chemistry SB RAS, 3 Akad. Lavrentiev Ave., 630090 Novosibirsk, Russia

² Institute of Natural Sciences and Mathematics, Ural Federal University Named after B.N. Yeltsin, 620075 Ekaterinburg, Russia

* Correspondence: abramov@niic.nsc.ru

Abstract: The affinity of $[\beta\text{-Mo}_8\text{O}_{26}]^{4-}$ toward different proton sources has been studied in various conditions. The proposed sites for proton coordination were highlighted with single crystal X-ray diffraction (SCXRD) analysis of $(\text{Bu}_4\text{N})_3[\beta\text{-}\{\text{Ag}(\text{py-NH}_2)\text{Mo}_8\text{O}_{26}\}]$ (1) and from analysis of reported structures. Structural rearrangement of $[\beta\text{-Mo}_8\text{O}_{26}]^{4-}$ as a direct response to protonation was studied in solution with ^{95}Mo NMR and HPLC-ICP-AES techniques. A new type of proton transfer reaction between $(\text{Bu}_4\text{N})_4[\beta\text{-Mo}_8\text{O}_{26}]$ and $(\text{Bu}_4\text{N})_4\text{H}_2[\text{V}_{10}\text{O}_{28}]$ in DMSO results in both polyoxometalates transformation into $[\text{V}_2\text{Mo}_4\text{O}_{19}]^{4-}$, which was confirmed by the ^{95}Mo , ^{51}V NMR and HPLC-ICP-AES techniques. The same type of reaction with $[\text{H}_4\text{SiW}_{12}\text{O}_{40}]$ in DMSO leads to metal redistribution with formation of $[\text{W}_2\text{Mo}_4\text{O}_{19}]^{2-}$.

Keywords: proton transfer; octamolybdate; NMR; chromatography; structural analysis



Citation: Volchek, V.V.; Kompankov, N.B.; Sokolov, M.N.; Abramov, P.A. Proton Affinity in the Chemistry of Beta-Octamolybdate: HPLC-ICP-AES, NMR and Structural Studies. *Molecules* **2022**, *27*, 8368. <https://doi.org/10.3390/molecules27238368>

Academic Editor: Xiaobing Cui

Received: 29 October 2022

Accepted: 25 November 2022

Published: 30 November 2022

Publisher's Note: MDPI stays neutral with regard to jurisdictional claims in published maps and institutional affiliations.



Copyright: © 2022 by the authors. Licensee MDPI, Basel, Switzerland. This article is an open access article distributed under the terms and conditions of the Creative Commons Attribution (CC BY) license (<https://creativecommons.org/licenses/by/4.0/>).

1. Introduction

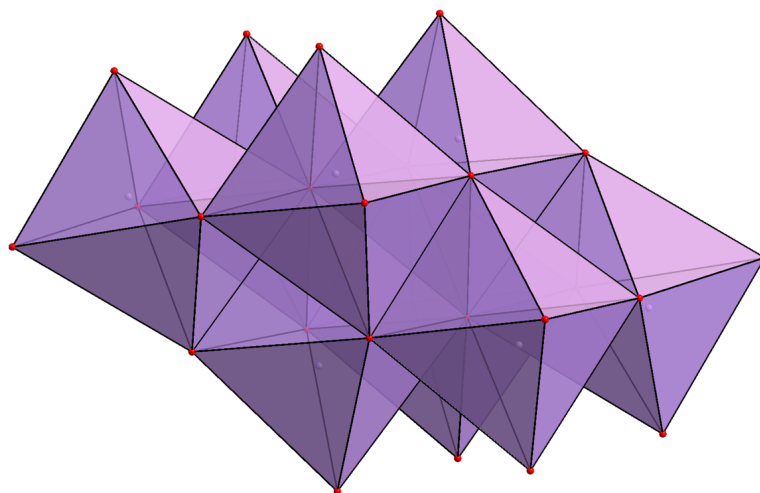
Protons play a key role in a wide range of water-associated processes, from geochemistry to biology [1]. The appearance of the Theory of Coupled Electron and Proton Transfer Reactions [2–4] opened rich prospects for chemical reactions design [5–8]. Currently, proton coupled electron transfer (PCET) processes play crucial roles in synthesis and catalysis [9,10], e.g., artificial photosynthesis systems [11–14] and PCET at interfaces [15–18].

In polyoxometalate (POM) chemistry, protonation affects the formation, stability and reactivity of polyoxoanions. Most self-assembly cascade reactions are pH driven when fast protonation-deprotonation processes provoke rapid species transformation/organization into various associates up to nanoscopic size. The study of self-assembly processes is one of the top subjects in modern chemical science [19–27]. Such a specific organization of the matter in different solutions is a research focus for a large number of research groups. For example, research groups led by T. Mak and Di Sun successfully merged polyoxometalate chemistry with that of coinage metal clusters using the self-assembly approach [28–30].

The electronic structure of polyoxoanions together with low-energy protonation makes such objects very attractive for PCET reactions. The most important catalytic process in this field is water oxidation [31,32]. Such POM catalysts as $[\{\text{Ru}^{\text{IV}}_4(\text{OH})_2(\text{H}_2\text{O})_4\}(\gamma\text{-SiW}_{10}\text{O}_{34})_2]^{10-}$ [33–35] and $[\text{Co}^{\text{II}}_4(\text{H}_2\text{O})_2(\text{B-}\alpha\text{-PW}_9\text{O}_{34})_2]^{10-}$ have become classics [36,37]. Recently, $[\text{V}_6\text{O}_{13}(\text{TRIOLO}_2)_2]^{2-}$ was applied to achieve concerted transfer of protons and electrons. Fully reduced clusters can induce $2e^-/2\text{H}^+$ transfer reactions from surface hydroxide ligands [38].

In the chemistry of group 6 polyoxometalates, the polyoxomolybdates are significantly more labile than the polyoxotungstates, thus making researchers favor the latter in their studies of POM chemistry. However, several studies of polyoxomolybdates' reactivity [39] and catalytic performance (electron transfer reactions) appeared [40–45]. One of the central complexes in this chemistry is $(\text{Bu}_4\text{N})_4[\beta\text{-Mo}_8\text{O}_{26}]$ (Scheme 1), which

is a standard precursor of all reactions in organic media, leading to a huge number of materials with different properties [46–49]. Our ongoing research focuses on the use of the coordination chemistry of the $[\beta\text{-Mo}_8\text{O}_{26}]^{4-}$ anion in the study of silver chemistry in non-aqueous solutions [50–52]. Karoui and Ritchie used $(\text{Bu}_4\text{N})_4[\beta\text{-Mo}_8\text{O}_{26}]$ in the microwave-assisted synthesis of tris(alkoxo)molybdovanadates $[\text{V}_3\text{Mo}_3\text{O}_{16}(\text{O}_3\text{-R})]^{2-}$ ($\text{R} = \text{C}_5\text{H}_8\text{OH}$ or $\text{C}_4\text{H}_6\text{NH}_2$) by the reaction between $[\beta\text{-Mo}_8\text{O}_{24}]^{4-}$, $[\text{H}_3\text{V}_{10}\text{O}_{28}]^{3-}$ and pentaerythritol or tris(hydroxymethyl)aminomethane [53]. These results show the possibility of the reaction between two different types of polyoxometalates producing mixed-metal compounds based on a different structural type. Such reactions are practically unknown and can generate interesting mixed metal complexes. This is very important and can be used for various materials preparation applied in catalysis (different Mo/V oxides), photochemistry, solid-state devices (capacitors), biochemistry and biomedicine.



Scheme 1. The structure of the $[\beta\text{-Mo}_8\text{O}_{26}]^{4-}$ anion.

An important question is what is the trigger and the driving force of such metal redistribution reactions? In this research, we focused on the behavior of the $[\beta\text{-Mo}_8\text{O}_{26}]^{4-}$ anion toward protonation to answer this question. Some years ago, we suggested a straightforward hyphenated HPCL-ICP-AES technique [54] as an efficient tool to study the reaction products in different polyoxometalate systems [55–57]. In the present research, this technique helps us to have control over products' formation in different conditions.

2. Results

2.1. Structural Analysis

The structure of $[\beta\text{-Mo}_8\text{O}_{26}]^{4-}$ is preorganized for the coordination of different metal cations due to the presence of two trans-located lacunes (Scheme 1). During the study of complexation in the $\text{Ag}^+ / [\beta\text{-Mo}_8\text{O}_{26}]^{4-} / \text{L}$ ($\text{L} =$ auxiliary ligand) systems [50,51,58], we found a large number of equilibria that can be easily shifted by the addition of different ligands. In the present case, we tested 4-aminopyridine (py-NH_2) as an auxiliary ligand in order to produce a 1D $\{-\text{Mo}_8\text{-Ag-py-NH}_2\text{-Ag-Mo}_8\text{-}\}$ coordination polymer. Instead of this, the reaction gives $(\text{Bu}_4\text{N})_3[\text{Ag}(\text{py-NH}_2)\text{Mo}_8\text{O}_{26}]$ as the main product (phase purity was confirmed by XRPD, see Supplementary Materials, Figure S1). In the crystal structure (SCXRD details are collected in Supplementary Materials Table S1) Ag^+ , $[\beta\text{-Mo}_8\text{O}_{26}]^{4-}$ and py-NH_2 combine into another type of 1D coordination polymer when $[\text{Ag}(\text{py-NH}_2)\text{Mo}_8\text{O}_{26}]^{3-}$ anions stack together via $\text{py-NH}_2 \dots \text{O}=\text{Mo}$ interactions (Figure 1).

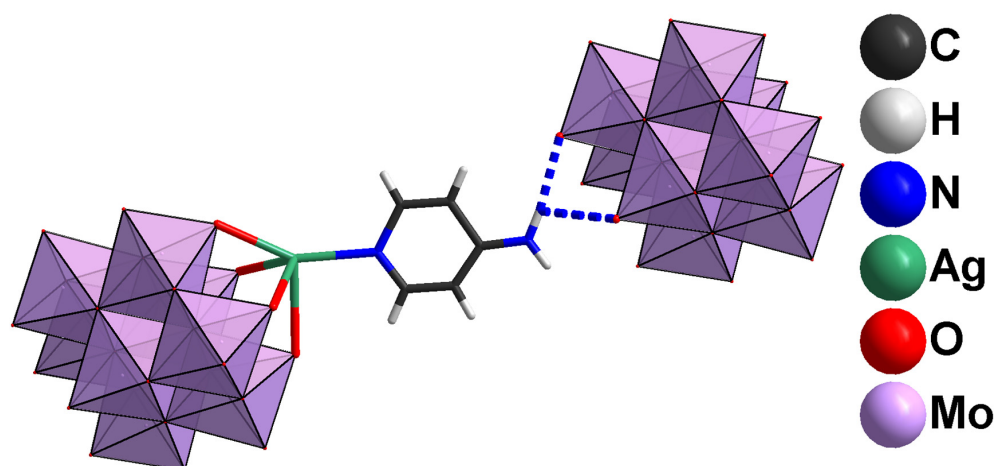


Figure 1. py-NH₂ ... O=Mo interactions in the crystal structure of 1.

Three typical bonding distances surround Ag⁺: $d(\text{Ag1-N1}) = 2.27(3) \text{ \AA}$, $d(\text{Ag1-O6}) = 2.372(7) \text{ \AA}$, $d(\text{Ag1-O2}) = 2.544(6) \text{ \AA}$ and two longer contacts $d(\text{Ag1-O9}) = 2.639(7) \text{ \AA}$ and $d(\text{Ag1-O13}) = 2.689(7) \text{ \AA}$ indicate CN = 3+2 for Ag⁺. These distances are in agreement with the previously published pyridinium complexes of this type [50]. The distances for py-NH₂ ... O=Mo interactions fill the interval between 2.974 and 3.285 Å. The shortest N ... O contacts 2.974 and 3.021 Å are depicted in blue in Figure 1.

The formation of this coordination polymer via NH₂ ... POM interactions is very interesting. We did the structural search for bonding between the oxoligands of the $[\beta\text{-Mo}_8\text{O}_{26}]^{4-}$ lacunes and H-atoms, and collected 11 hits (BURBOH, CASNIU, COPFIW, EWILIG, GEBYER, GISHEW, HIJSUR, MAXPUZ, MEPNIH, VEHTAF, YAGNOJ) from CCDC (ConQuest Version 2020.2.0). We will use the corresponding refcodes of deposited crystal structures as references in the description below.

The interactions between $[\beta\text{-Mo}_8\text{O}_{26}]^{4-}$ and Me₂NH(R), Me₂NH₂⁺ and NH₄⁺ in the crystal structures of YAGNOJ (a); BURBOH (b); HIJSUR (c); GISHEW (d) are shown in Figure 2.

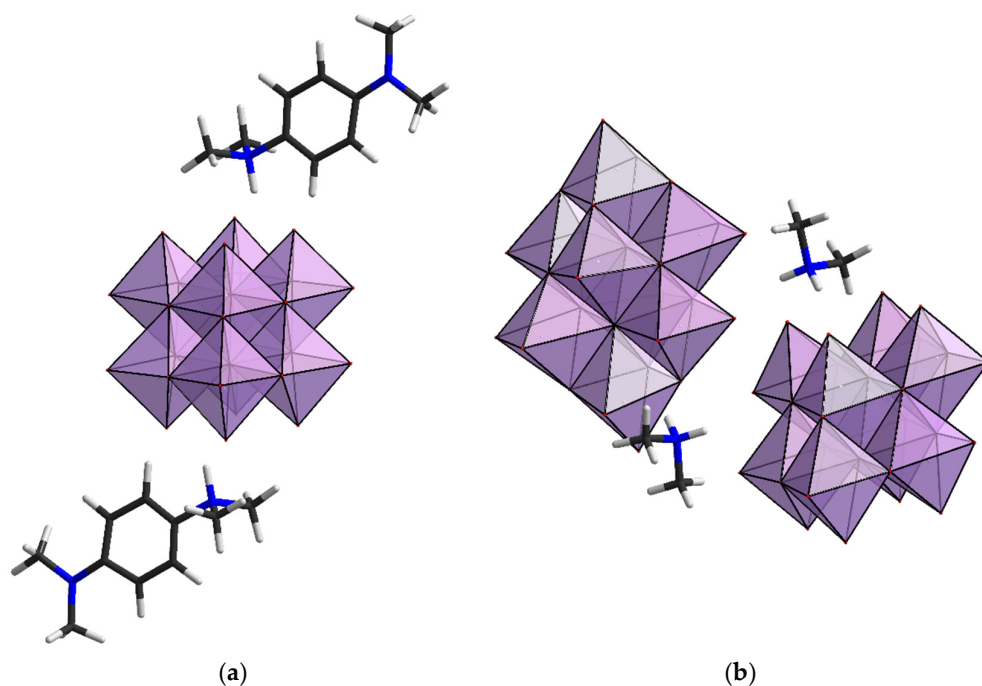


Figure 2. Cont.

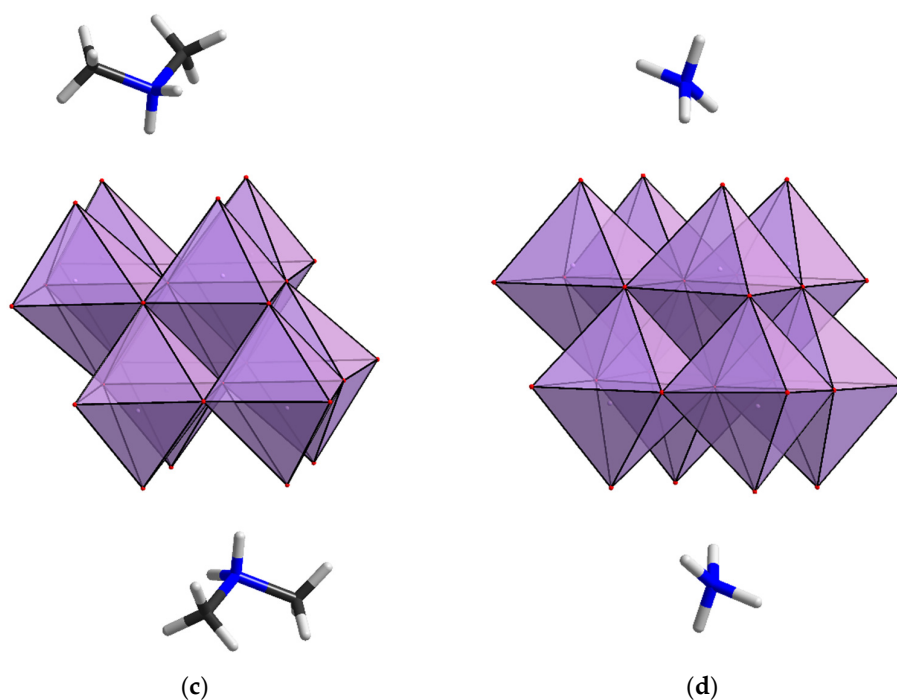


Figure 2. H...O=Mo interactions in the crystal structure of: (a) YAGNOJ; (b) BURBOH; (c) HIJSUR; (d) GISHEW.

According to the structural analysis, R_3NH^+ , $R_2NH_2^+$ and NH_4^+ interact with terminal O=Mo groups of $[\beta-Mo_8O_{26}]^{4-}$ lacunes. Moreover, even Me_4N^+ can interact with the lacune (VEHTAF). In the crystal structure of GEBYER, the $[\beta-Mo_8O_{26}]^{4-}$ lacunes interact with two H_2O molecules. In the case of **1**, we detected interaction between the neutral NH_2 -group protons with the O=Mo groups of polyoxomolybdate. This illustrates strong attraction between the lacune terminal oxoligands and H-atoms possessing some acidity (chiefly N–H, but also C–H in Me_4N^+). Considering this, we can suggest direct proton transfer exactly to these oxoligands-producing terminal Mo–OH group, which is highly reactive (M–O π -bonding breaking) and initiates further rearrangement of octamolybdate into hexamolybdate. The detailed mechanistic studies of this transformation are still absent. In this research, we used this channel to initiate the reaction between $[\beta-Mo_8O_{26}]^{4-}$ and different protonated polyoxometalates serving as proton source. Such direct reactions between two different polyoxometalates are poorly studied. The HPLC-ACP-AES technique was used to control the products.

2.2. Reactivity of $[\beta-Mo_8O_{26}]^{4-}$

The first candidate for this type of reaction was easily prepared $(Bu_4N)_4H_2[V_{10}O_{28}]$. The HPLC-ICP-AES chromatogram of pure $(Bu_4N)_4[\beta-Mo_8O_{26}]$ in acetonitrile shows a major molybdenum peak ($t_R = 3.6$ min), corresponding to the octamolybdate anion $[\beta-Mo_8O_{26}]^{4-}$, and a minor peak ($t_R = 4.8$ min), which can be assigned as a hexamolybdate anion $[Mo_6O_{19}]^{2-}$ (Figure 3a) [59]. The profile of the major peak is asymmetric due to the presence of $[\alpha-Mo_8O_{26}]^{4-}$, according to the previous ESI-MS data, demonstrating the absence of any other molybdates in the solution [50]. The HPLC-ICP-AES chromatogram of a freshly prepared solution of $(Bu_4N)_4H_2[V_{10}O_{28}]$ shows a single peak containing vanadium ($t_R = 3.0$ min), which confirms the presence of individual vanadate anion $[V_{10}O_{28}]^{6-}$ in the solution (Figure 3b). Moreover, the addition of 2 eq of Bu_4NOH to the solution of $(Bu_4N)_4H_2[V_{10}O_{28}]$ does not reflect any POM transformation.

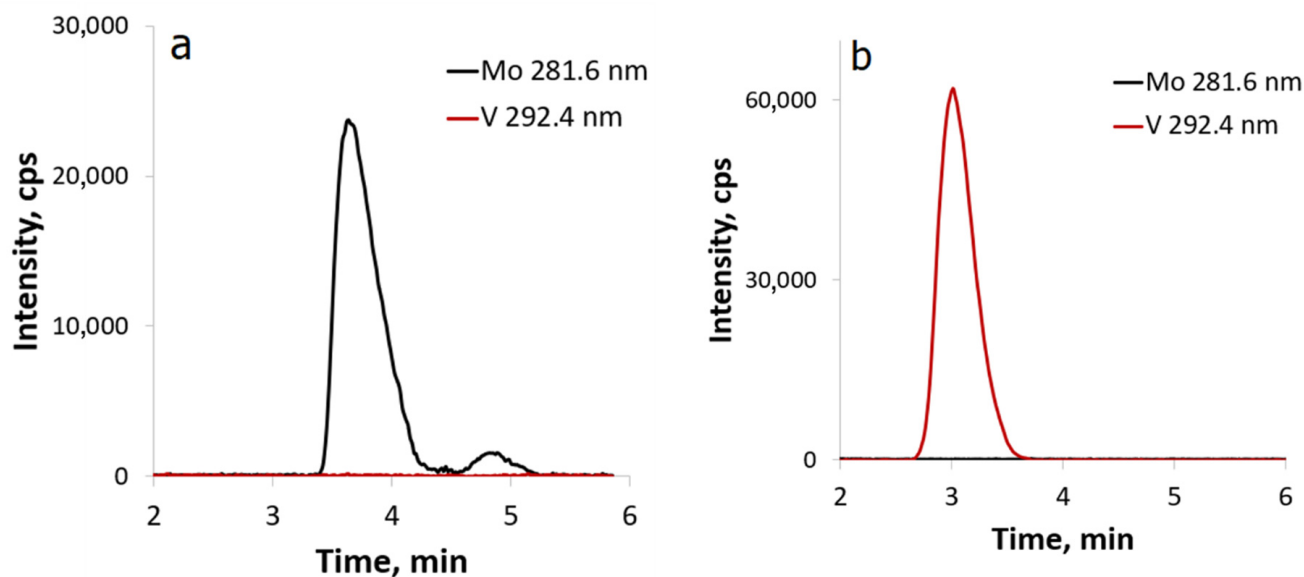


Figure 3. HPLC-ICP-AES chromatograms of (a) $[\beta\text{-Mo}_8\text{O}_{26}]^{4-}$ and (b) $[\text{V}_{10}\text{O}_{28}]^{6-}$ in acetonitrile.

The reaction between $(\text{Bu}_4\text{N})_4[\beta\text{-Mo}_8\text{O}_{26}]$ and $(\text{Bu}_4\text{N})_4\text{H}_2[\text{V}_{10}\text{O}_{28}]$ in DMSO does not proceed at room temperature, according to ^{51}V NMR data, which is the fastest way to check the reaction progress. The reaction mixture must be heated over 50°C to activate the polyoxometalates' transformation. The HPLC-ICP-AES technique was used to investigate the reaction products at different molar ratios of the reagents. The reaction time was 10 min.

For molar ratio 5/1 (Mo:V = 5/1) at C_0 of $(\text{Bu}_4\text{N})_4[\beta\text{-Mo}_8\text{O}_{26}] = 6\text{ mM}$, we observed one peak with the atomic ratio Mo:V = 2.2 ($t_R = 4.3\text{ min}$) (Figure 4a) and a second V-free peak ($t_R = 4.8\text{ min}$), which may be ascribed to unreacted octamolybdate (Figure 4a). With an increase in the vanadate concentration (Mo/V = 5:2 molar ratio), the same major peak with atomic ratio Mo:V = 2.5 was observed, the intensity of which doubled (Figure 4b). In addition, a chromatogram shows a minor Mo-free peak ($t_R = 3.0\text{ min}$), which indicates an excess of the decavanadate anion in this case (Figure 3b).

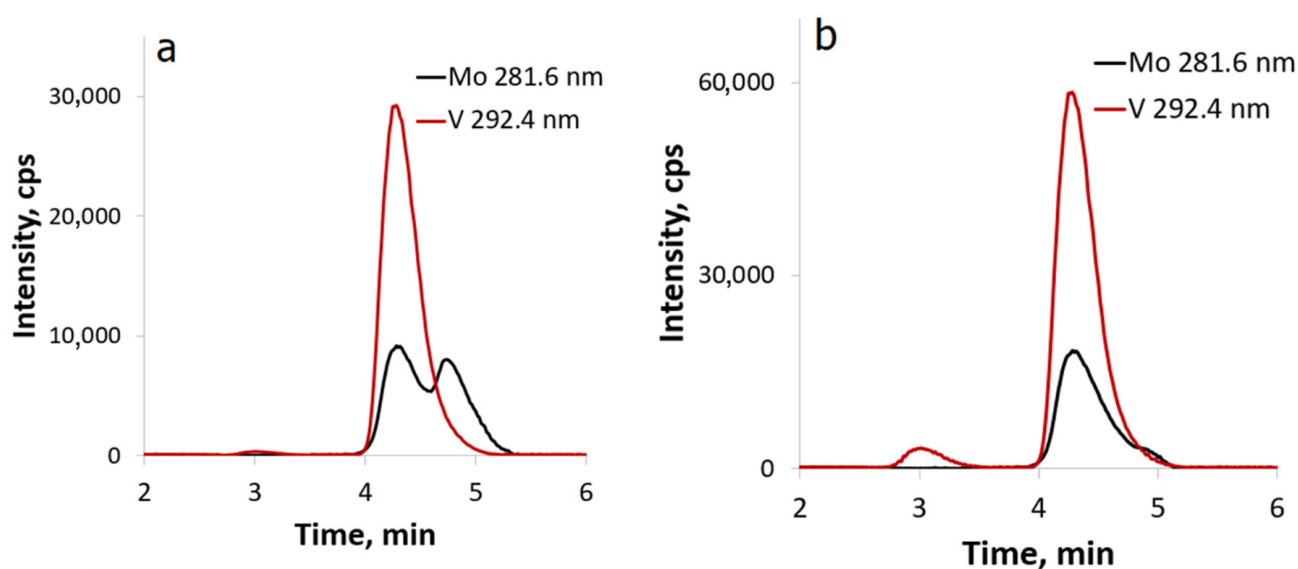


Figure 4. HPLC-ICP-AES chromatograms of the POM mixture at (a) the initial Mo/V ratio = 5/1 and (b) Mo/V ratio = 5/2.

No significant changes in the chromatograms were observed with a further increase in the concentration of vanadate. The atomic ratio Mo:V = 2.2 indicates the formation of $[V_2Mo_4O_{19}]^{4-}$ Lindqvist type anions as the reaction product. According to ^{51}V NMR, the total intensity of the other V peaks is ca. 1% of the intensity of the signal from the major product (See NMR part).

The next candidate to study the proton transfer controlled reaction with $(Bu_4N)_4[\beta-Mo_8O_{26}]$ was $[H_4SiW_{12}O_{40}] \cdot 14H_2O$. Preliminary experiments showed that the reaction between $(Bu_4N)_4[\beta-Mo_8O_{26}]$ and $[H_4SiW_{12}O_{40}] \cdot 14H_2O$ in acetonitrile proceeded slowly and led to the formation of a number of products in comparable amounts. Therefore, CH_3CN was replaced with dimethyl sulfoxide (DMSO). The HPLC-ICP-AES chromatogram of a freshly prepared solution of silicotungstic acid in DMSO shows a single peak containing tungsten ($t_R = 6.2$ min), which confirms the presence of individual silicotungstate anion $[SiW_{12}O_{40}]^{4-}$ in the solution (Figure 5a) (The intensities of Si lines are significantly lower than W or Mo and cannot be adequately estimated).

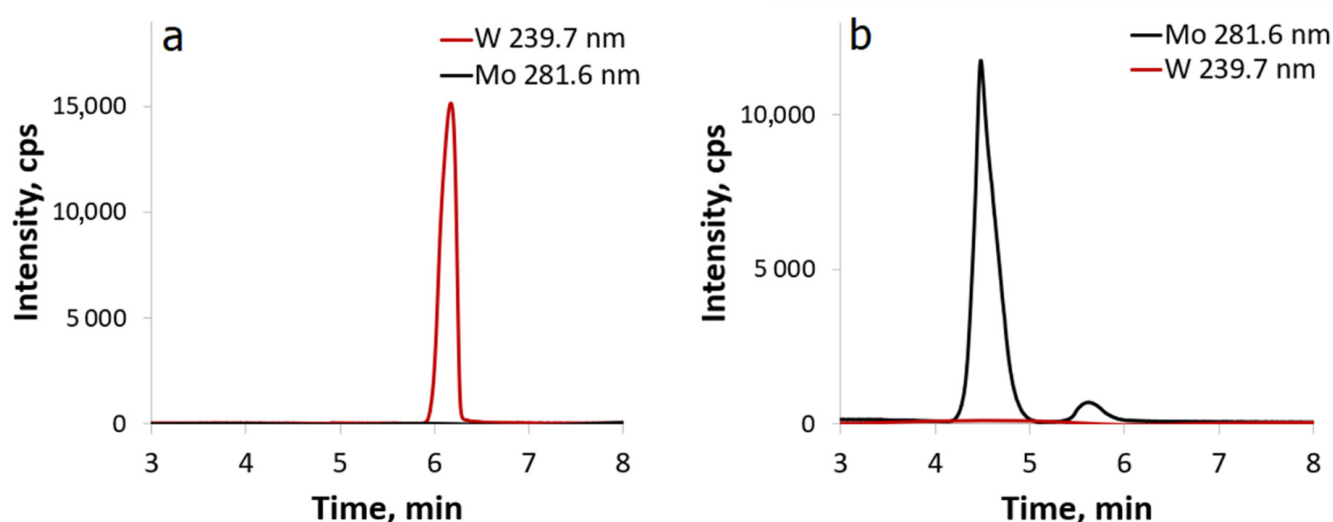


Figure 5. HPLC-ICP-AES chromatograms of (a) $[SiW_{12}O_{40}]^{4-}$ and (b) $[\beta-Mo_8O_{26}]^{4-}$ in dimethyl sulfoxide.

The HPLC-ICP-AES chromatogram of $(Bu_4N)_4[\beta-Mo_8O_{26}]$ in DMSO (Figure 5b) is similar to the chromatogram in acetonitrile (Figure 3a) and shows a major molybdenum peak ($t_R = 4.5$ min), corresponding to the octamolybdate anion $[\beta-Mo_8O_{26}]^{4-}$, and a minor peak of $[Mo_6O_{19}]^{2-}$ [59]. Since the viscosity of DMSO is 5 times that of acetonitrile, we were forced to reduce the concentration of the ion-pair reagent in the HPLC eluent to prevent column overpressure. Therefore, the peak retention times in DMSO increased. The HPLC-ICP-AES technique was used to investigate the reaction products between $(Bu_4N)_4[\beta-Mo_8O_{26}]$ and $[H_4SiW_{12}O_{40}] \cdot 14H_2O$ at different molar ratios. For the Mo/W = 10/1 molar ratio at C_0 of $(Bu_4N)_4[\beta-Mo_8O_{26}] = 3$ mM, we observed four peaks (Figure 6a): (i) unreacted octamolybdate ($t_R = 4.5$ min), (ii) poorly separated peak with atomic ratio Mo:W = 2.3 ($t_R = 4.7$ min), (iii) hexamolybdate ($t_R = 5.7$ min) and (iv) Mo-free peak ($t_R = 6.2$ min) from unreacted silicotungstic acid. With an increase in the tungstate concentration (Mo/W = 10/2 molar ratio), the same major peak with atomic ratio Mo:W = 2.3 was observed (Figure 6b). In addition, the chromatogram shows minor W-free peaks ($t_R = 4.5$ min, $t_R = 5.6$ min) and a single peak containing tungsten ($t_R = 6.2$ min), which may indicate an excess of the tungstate anion. Further increase in the concentration of tungstate (Mo/W = 10/4 molar ratio) leads to the disappearance of the first molybdenum peak ($[\beta-Mo_8O_{26}]^{4-}$, $t_R = 4.5$ min) and an increase in the intensity of the peak of unreacted tungstate.

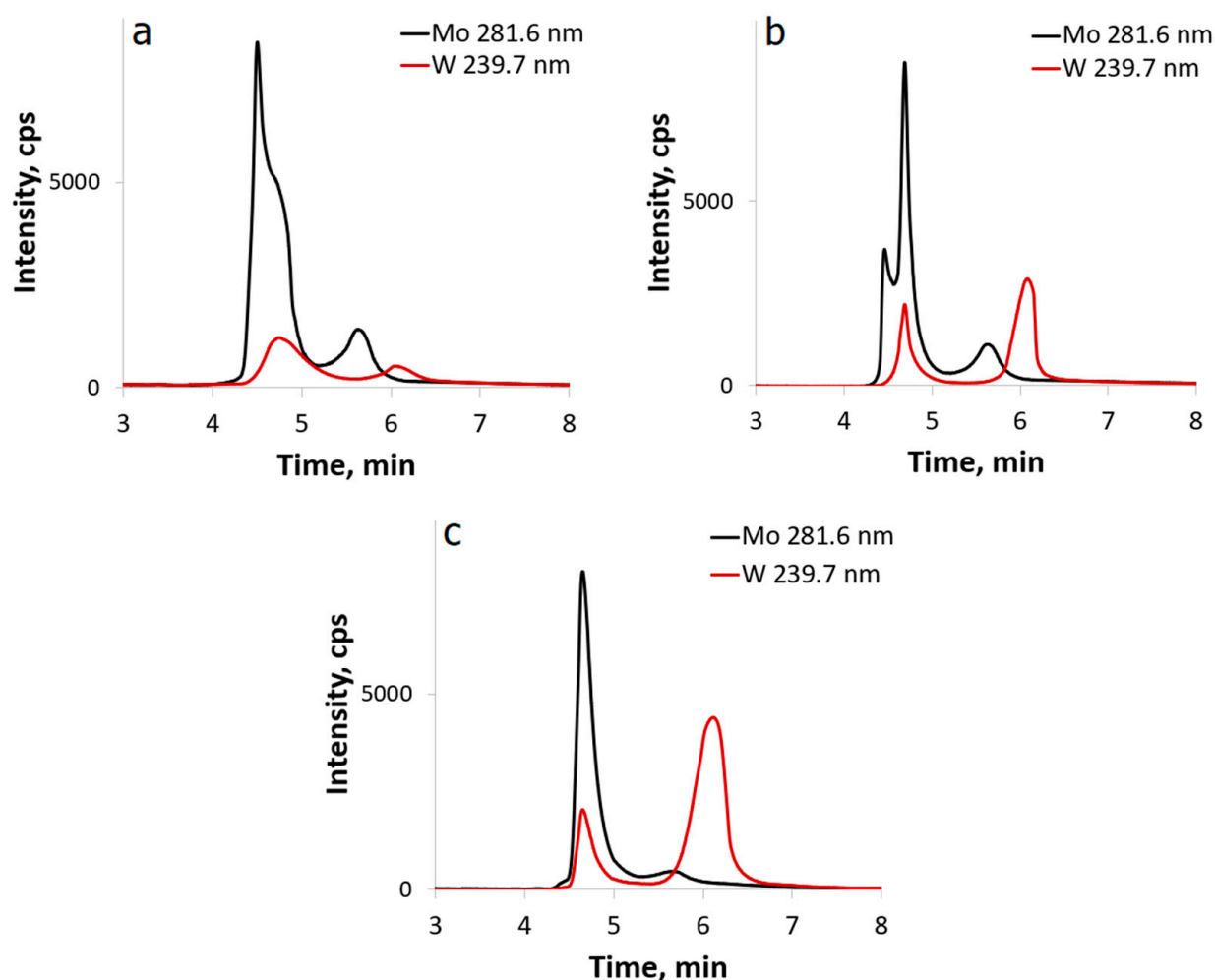


Figure 6. HPLC-ICP-AES chromatograms of the POM mixture at (a) the initial Mo/W ratio = 10/1, (b) Mo/W ratio = 10/2 and (c) Mo/W ratio = 10/4.

Thus, according to the HPLC-ICP-AES results, the proton transfer between the silicotungstic acid and $[\beta\text{-Mo}_8\text{O}_{26}]^{4-}$ triggers metal redistribution with the formation of Lindqvist type $[\text{W}_2\text{Mo}_4\text{O}_{19}]^{2-}$ anion as the reorganization product of $[\beta\text{-Mo}_8\text{O}_{26}]^{4-}$. Curiously, $[\alpha\text{-Mo}_8\text{O}_{26}]^{4-}$ does not react in this case. The Keggin anion almost completely converts into the mixed Lindqvist at Mo/W ratio = 10/1 (Figure 6a). We reported a similar process earlier, when direct reaction of $[\text{H}_3\text{PW}_{12}\text{O}_{40}]$ with $[\text{NbO}(\text{C}_2\text{O}_4)_2]^-$ yielded $[\text{PW}_{11}\text{NbO}_{40}]^{4-}$ [60].

The reaction between $(\text{Bu}_4\text{N})_4[\beta\text{-Mo}_8\text{O}_{26}]$ and acetic acid was investigated with the HPLC technique. The reaction was run in DMSO (C_0 of = 3 mM) by the addition of various concentrations of acetic acid (Figure 7).

The HPLC chromatogram of a freshly prepared solution of $(\text{Bu}_4\text{N})_4[\beta\text{-Mo}_8\text{O}_{26}]$ shows the peaks from octamolybdate $[\beta\text{-Mo}_8\text{O}_{26}]^{4-}$ (Figure 5, peak no. 3, $t_R = 4.5$ min) and hexamolybdate $[\text{Mo}_6\text{O}_{19}]^{2-}$ (Figure 7, peak no. 5, $t_R = 5.6$ min) in the ratio of 95:5. Addition of 0.001 M acetic acid decreases the octamolybdate peak intensity, while causing an increase in the hexamolybdate peak intensity and the appearance of a new peak (peak no. 4, $t_R = 5.1$ min). Further increase in the acetic acid concentration continues to reduce the intensity of the octamolybdate peak and leads to an increase in the intensity of peak no. 4, as well as the appearance of two minor peaks (peak no. 1,2) of smaller molybdates. At an acetic acid concentration of 0.008 M, the intensity ratio of the peaks corresponding to octamolybdate (peak no. 3), the new product (peak no. 4), and hexamolybdate (peak no. 5), is 1.8:3.4:1, respectively. No further changes in the ratio of species in solution was observed

with an increase in the concentration of acetic acid from 0.008 M to 0.01 M; however, the intensity of all peaks decreases by 1.5, and further acidification leads to the formation of a white precipitate, which makes the HPLC analysis unapplicable.

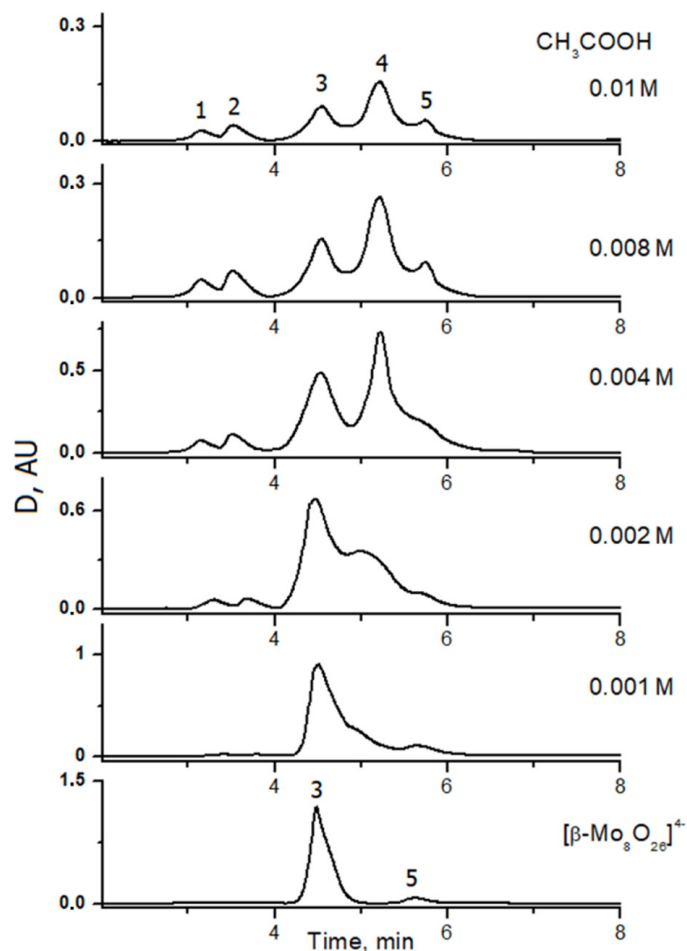


Figure 7. The HPLC-UV chromatograms of $(\text{Bu}_4\text{N})_4[\beta\text{-Mo}_8\text{O}_{26}]$ in dimethyl sulfoxide with the addition of acetic acid.

From this observation it follows that the transformation of $[\beta\text{-Mo}_8\text{O}_{26}]^{4-}$ into $[\text{Mo}_6\text{O}_{19}]^{2-}$ can be explained as direct dimolybdate ($[\text{Mo}_2\text{O}_7]^{2-}$) elimination, as was proposed earlier. There are two simple molybdate anions in the reaction mixture. In the literature there is a structure of $\text{K}[\text{MoO}_2(\text{OAc})_3]\cdot\text{HOAc}$ [61] complex, showing the possibility of $[\text{MoO}_2(\text{OAc})_3]^-$ existence in the solution. The new peak (Figure 7, peak no. 4) can be assigned as $[\text{Mo}_8\text{O}_{24}(\text{OAc})_2]^{4-}$, with the same structure as reported for the malonate derivative $(\text{NH}_4)_4[\text{Mo}_8\text{O}_{24}(\text{C}_3\text{H}_2\text{O}_2)_2]\cdot 4\text{H}_2\text{O}$ [62].

2.3. NMR

NMR spectroscopy was anticipated to be an informative tool to study the reaction between $(\text{Bu}_4\text{N})_4[\beta\text{-Mo}_8\text{O}_{26}]$ (**Mo8**) and $(\text{Bu}_4\text{N})_4\text{H}_2[\text{V}_{10}\text{O}_{28}]$ (**V10**) due to the presence of both ^{51}V and ^{95}Mo NMR active isotopes. We measured ^{95}Mo NMR spectra for the following solutions to study the effects of acidification of **Mo8** by Hpts (Hpts = *p*-toluenesulfonic acid) (Figure 8).

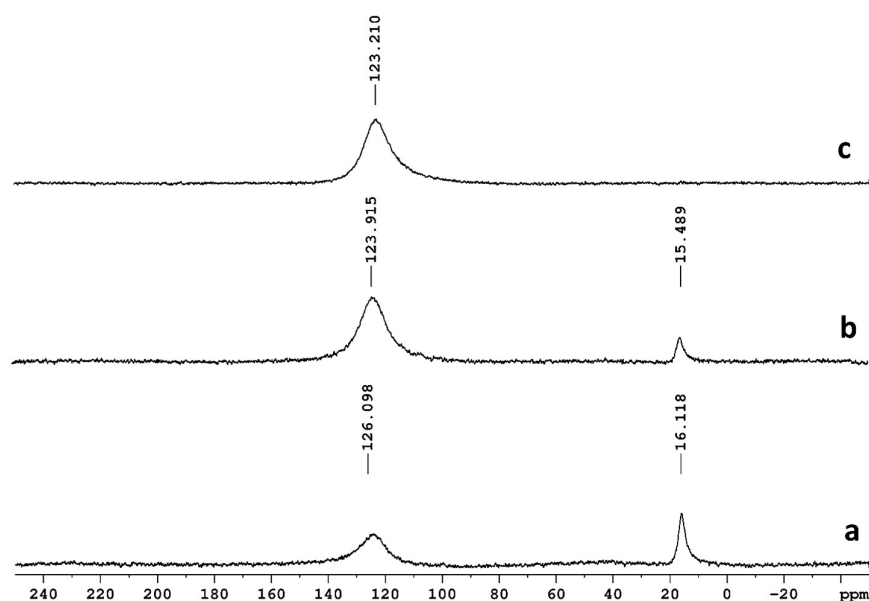


Figure 8. ^{95}Mo NMR data for **Mo8** acidification: (a) 70 mg **Mo8** + 2 mg of Hpts in 600 μL $\text{DMSO-}d_6$; (b) 70 mg **Mo8** + 5 mg of Hpts in 600 μL $\text{DMSO-}d_6$; (c) 70 mg **Mo8** + 10 mg of Hpts in 600 μL $\text{DMSO-}d_6$.

As can be seen, addition of Hpts as a non-coordinating organic acid to the solution of $(\text{Bu}_4\text{N})_4[\beta\text{-Mo}_8\text{O}_{26}]$ leads to the disappearance of the $[\alpha\text{-Mo}_8\text{O}_{26}]^{4-}$ isomer and an increase in the amount of $[\text{Mo}_6\text{O}_{19}]^{2-}$. Simple (mononuclear or binuclear) Mo-containing complexes were not detected, most likely due to the fast exchange. The signals from such species should appear in a negative region, in comparison with the literature [63].

The reaction between **Mo8** and **V10** was studied using both ^{95}Mo and ^{51}V NMR (Figure 9).

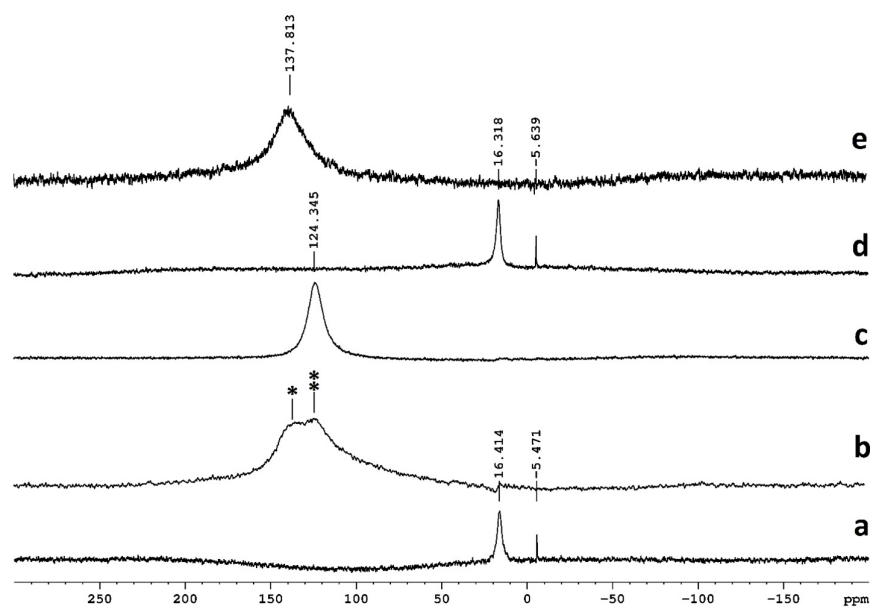


Figure 9. ^{95}Mo NMR data describing **Mo8** and **V10** reaction: (a) 70 mg **Mo8** (300 μL $\text{DMSO-}d_6$) + 55 mg **V10** (300 μL $\text{DMSO-}d_6$) room temperature; (b) 70 mg **Mo8** (300 μL $\text{DMSO-}d_6$) + 22 mg **V10** (300 μL $\text{DMSO-}d_6$), after 10 min at 60 $^\circ\text{C}$; (c) 70 mg $(\text{Bu}_4\text{N})_2[\text{Mo}_6\text{O}_{19}]$ in 600 μL $\text{DMSO-}d_6$; (d) 70 mg **Mo8** in 600 μL $\text{DMSO-}d_6$; (e) 70 mg of $(\text{Bu}_4\text{N})_3\text{Na}[\text{V}_2\text{Mo}_4\text{O}_{19}]$ in 600 μL $\text{DMSO-}d_6$ * Chemical shift (CS) = 137.4301 ppm, ** CS = 123.3993 ppm.

The ^{51}V NMR spectra (Figures S2–S4) show exclusive formation of $[\text{V}_2\text{Mo}_4\text{O}_{19}]^{4-}$, to the detriment of other mixed metal Lindqvist molybdovanadates, meaning that such reactions can offer a straightforward way to this anion. Two signals in the ^{95}Mo NMR spectrum of $(\text{Bu}_4\text{N})_4[\beta\text{-Mo}_8\text{O}_{26}]$ indicate an equilibrium between α and β isomers, as described in the literature [64]. In the case of spectrum *b* (Figure 9), the baseline correction was not as accurate, and the peaks from **Mo8** have slightly negative intensities. Moreover, due to this problem, the profile of the main signal is also not as correct. Nevertheless, we can postulate the presence of $[\text{V}_2\text{Mo}_4\text{O}_{19}]^{4-}$ and $[\text{Mo}_6\text{O}_{19}]^{2-}$ in the reaction mixture.

3. Materials and Methods

3.1. Physical Methods

$(\text{Bu}_4\text{N})_4[\beta\text{-Mo}_8\text{O}_{26}]$, $(\text{Bu}_4\text{N})_2[\text{Mo}_6\text{O}_{19}]$, $(\text{Bu}_4\text{N})_2[\text{Mo}_2\text{O}_7]$, $(\text{Bu}_4\text{N})_4\text{H}_2[\text{V}_{10}\text{O}_{28}]$ and $(\text{Bu}_4\text{N})_3\text{Na}[\text{V}_2\text{Mo}_4\text{O}_{19}]$ were prepared according to the literature data (Inorg. Synth. Vol. 27). DMSO was distilled in vacuo over NaOH. $[\text{H}_4\text{SiW}_{12}\text{O}_{40}] \cdot 14\text{H}_2\text{O}$ was manufactured by “The Red Chemist” (Saint Petersburg, USSR) and checked with FT-IR and TGA prior to use. Other reagents were of commercial quality (Sigma Aldrich) and were used as purchased. IR spectra were recorded on a Bruker Vertex 60 FT-IR spectrometer. Elemental analysis was carried out on a MICRO Cube CHN analyzer.

Synthesis of $(\text{Bu}_4\text{N})_3[\text{Ag}(\text{py-NH}_2)\text{Mo}_8\text{O}_{26}]$ (1**):** $(\text{Bu}_4\text{N})_4[\beta\text{-Mo}_8\text{O}_{26}]$ (200 mg, mmol) was dissolved in 2 mL of DMF under sonication, and afterward, 20 mg (mmol) of py-NH₂ was added to the observed clear solution. Solid AgNO₃ (32 mg, mmol) was added to the reaction mixture under sonication. The resulting mixture was placed in Et₂O atmosphere at 4 °C to obtain crystalline material. The crop of large colorless crystals was isolated after 48 h. Yield was 175 mg (90% based on initial octamolybdate).

Elemental analysis. Calcd C, H, N (%) for **1**: 30.1, 5.4, 3.3; found C, H, N (%): 30.0, 5.3, 3.2.

IR (KBr, cm^{-1}): 3485 (w), 3336 (m), 3222 (w), 2959 (vs), 2929 (s), 2872 (s), 1632 (vs), 1611 (s), 1554 (w), 1522 (m), 1480 (vs), 1456 (s), 1375 (m), 1355 (w), 1333 (w), 1278 (w), 1214 (m), 1148 (w), 1100 (w), 1060 (w), 1028 (w), 1014 (m), 970 (s), 947 (vs), 928 (vs), 905 (vs), 865 (vs), 847 (vs), 825 (s), 811 (m), 700 (vs), 657 (vs), 567 (m), 551 (s), 520 (s), 472 (m), 444 (w), 407 (s).

3.2. NMR

^{51}V and ^{95}Mo NMR spectra were recorded on a Bruker Avance III 500 spectrometer (BBI detector), using NaVO₃ and Na₂MoO₄ as internal standards. Spectra were measured in DMSO-*d*₆ at room temperature using standard 5 mm NMR tubes.

3.3. X-ray Diffraction on Single Crystals

Crystallographic data and refinement details are given in Table S1 (Supplementary Materials). The diffraction data for **1** were collected on a Bruker D8 Venture diffractometer with a CMOS PHOTON III detector and I μ S 3.0 source (Mo K α radiation, $\lambda = 0.71073$ Å) at 150 K. The φ - and ω -scan techniques were employed. Absorption correction was applied by SADABS (Bruker Apex3 software suite: Apex3, SADABS-2016/2 and SAINT, version 2018.7-2; Bruker AXS Inc.: Madison, WI, USA, 2017). Structures were solved by SHELXT [65] and refined by full-matrix least-squares treatment against $|F|^2$ in anisotropic approximation with SHELX 2014/7 [66] in the ShelXle program [67]. H-atoms were refined in geometrically calculated positions.

CCDC 2215910 contains the supplementary crystallographic data. These data can be obtained free of charge via <http://www.ccdc.cam.ac.uk/conts/retrieving.html>, or from the Cambridge Crystallographic Data Centre, 12 Union Road, Cambridge CB2 1EZ, UK; fax: (+44) 1223-336-033; or e-mail: deposit@ccdc.cam.ac.uk.

3.4. XRPD

X-ray powder diffraction patterns were measured on a Bruker D8 Advance diffractometer using LynxEye XE T-discriminated $\text{CuK}\alpha$ radiation. Samples were layered on a flat plastic specimen holder.

3.5. HPLC-ICP-AES and HPLC

Separation was performed with the HPLC system Milichrom A-02 (EcoNova, Novosibirsk, Russia), equipped with a two-beam spectrophotometric detector at the wavelength range of 190–360 nm in the ion-pair mode of reversed phase chromatography (Pron-toSIL 120-5-C18AQ, 2×75 mm), eluents: A—0.06% tetrabutylammonium hydroxide (for $(\text{Bu}_4\text{N})_4[\beta\text{-Mo}_8\text{O}_{26}]$ and $(\text{Bu}_4\text{N})_4\text{H}_2[\text{V}_{10}\text{O}_{28}]$), 0.02% tetrabutylammonium hydroxide (for $(\text{Bu}_4\text{N})_4[\beta\text{-Mo}_8\text{O}_{26}]$ and $[\text{H}_4\text{SiW}_{12}\text{O}_{40}] \cdot 14\text{H}_2\text{O}$); B—acetonitrile. Gradient elution with a gradual increase in acetonitrile concentration was employed to resolve the species. ICP-AES spectrometer iCap 6500 Duo (Thermo Scientific, Waltham, MA, USA) with concentric nebulizer was applied as detector in hyphenated HPLC-ICP-AES. For the element detection Mo 281.6 nm, V 292.4 nm and W 239.7 nm, spectral lines were selected. All measurements were performed in three replicates.

The data acquisition and processing were carried out with iTEVA (Thermo Scientific, Waltham, MA, USA) software. In order to eliminate plasma quenching, we diluted the liquid coming out of the column into the spray chamber with deionized water. The steady state of the plasma and the optimal values of the analytical signals were finally achieved at the eluent flow rate of 0.25 mL min^{-1} and the eluent velocity of 3 mL min^{-1} (peristaltic pump speed—75 rpm).

4. Conclusions

This manuscript describes an affinity of $[\beta\text{-Mo}_8\text{O}_{26}]^{4-}$ lacunes for interaction with H-atoms possessing some N–H or even C–H (in Me_4N^+) acidity. We demonstrated this in the case of 1D polymeric chains formation via py-NH₂ and $[\beta\text{-Mo}_8\text{O}_{26}]^{4-}$ interaction. This example illustrates a general approach to the formation of soft matters based on such types of interactions. The reaction of $[\beta\text{-Mo}_8\text{O}_{26}]^{4-}$ with diluted acids generates a set of unknown complexes, according to the HPLC-ICP-AES data. Moreover, there was a new type of reactivity of $[\beta\text{-Mo}_8\text{O}_{26}]^{4-}$ combining: (i) proton transfer from another type of polyoxometalates in solution, (ii) backbone breaking and (iii) transformation into mixed Lindqvist type complexes has been demonstrated. In the case of $(\text{Bu}_4\text{N})_4\text{H}_2[\text{V}_{10}\text{O}_{28}]$, this reaction gives $[\text{V}_2\text{Mo}_4\text{O}_{19}]^{4-}$. $[\text{H}_4\text{SiW}_{12}\text{O}_{40}]$ plays a role as a proton and W source, producing $[\text{W}_2\text{Mo}_4\text{O}_{19}]^{2-}$. The key study here is proton transfer into the lacune of $[\beta\text{-Mo}_8\text{O}_{26}]^{4-}$, generating the reactive transition state. At the current stage, it is impossible to deduce the mechanism, which is not as simple as $[\text{Mo}_2\text{O}_7]^{2-}$ -elimination. In comparison with the microwave synthesis reported by Karoui and Ritchie, simple thermal activation does not need any special equipment. The addition of any triol type organic ligands into the reaction mixture will be the next step in such reactivity studies. Such an approach opens a way to new mixed functionalized complexes.

Supplementary Materials: The following supporting information can be downloaded at: <https://www.mdpi.com/article/10.3390/molecules27238368/s1>, Table S1: SCXRD Experimental details; Figure S1: Comparison of experimental and calculated powder diffraction patterns for **1**; Figure S2: ⁵¹V NMR spectrum of $(\text{Bu}_4\text{N})_3\text{Na}[\text{V}_2\text{Mo}_4\text{O}_{19}]$ (DMSO-*d*₆, r.t.); Figure S3: ⁵¹V NMR spectrum of the reaction mixture containing 70 mg **Mo8** (300 μL DMSO-*d*₆) + 55 mg **V10** (300 μL DMSO-*d*₆); Figure S4: ⁵¹V NMR spectrum of the reaction mixture containing 70 mg **Mo8** (300 μL DMSO-*d*₆) + 22 mg **V10** (300 μL DMSO-*d*₆), after 10 min at 60 °C.

Author Contributions: Conceptualization, P.A.A.; methodology, P.A.A.; validation, P.A.A., V.V.V. and N.B.K.; formal analysis, V.V.V. and N.B.K.; data curation, V.V.V. and N.B.K.; writing—original draft preparation, P.A.A.; writing—review and editing, P.A.A. and M.N.S.; visualization, V.V.V. and N.B.K.; supervision, P.A.A.; project administration, P.A.A.; funding acquisition, P.A.A. All authors have read and agreed to the published version of the manuscript.

Funding: This work was supported by the grant of the President of the Russian Federation for young scientists—Doctors of Sciences MD-396.2021.1.3.

Institutional Review Board Statement: Not applicable.

Informed Consent Statement: Not applicable.

Data Availability Statement: The crystallographic data have been deposited in the Cambridge Crystallographic Data Centre under the deposition codes CCDC 2215910.

Acknowledgments: The authors thank the Ministry of Science and Higher Education of the Russian Federation for access to the XRD facilities of the Nikolaev Institute of Inorganic Chemistry. The technical staff of the Institute is also thanked for their assistance.

Conflicts of Interest: The authors declare no conflict of interest. The funders had no role in the design of the study; in the collection, analyses, or interpretation of data; in the writing of the manuscript; or in the decision to publish the results.

References

1. Ishikita, H.; Saito, K. Proton transfer reactions and hydrogen-bond networks in protein environments. *J. R. Soc. Interface* **2014**, *11*, 20130518. [[CrossRef](#)] [[PubMed](#)]
2. Mayer, J.M. Proton-Coupled Electron Transfer: A Reaction Chemist's View. *Annu. Rev. Phys. Chem.* **2004**, *55*, 363–390. [[CrossRef](#)] [[PubMed](#)]
3. Hammes-Schiffer, S.; Stuchebrukhov, A.A. Theory of Coupled Electron and Proton Transfer Reactions. *Chem. Rev.* **2010**, *110*, 6939–6960. [[CrossRef](#)] [[PubMed](#)]
4. Chang, C.J.; Chang, M.C.Y.; Damrauer, N.H.; Nocera, D.G. Proton-coupled electron transfer: A unifying mechanism for biological charge transport, amino acid radical initiation and propagation, and bond making/breaking reactions of water and oxygen. *Biochim. Biophys. Acta—Bioenerg.* **2004**, *1655*, 13–28. [[CrossRef](#)] [[PubMed](#)]
5. Tyburski, R.; Liu, T.; Glover, S.D.; Hammarström, L. Proton-Coupled Electron Transfer Guidelines, Fair and Square. *J. Am. Chem. Soc.* **2021**, *143*, 560–576. [[CrossRef](#)]
6. Darcy, J.W.; Koronkiewicz, B.; Parada, G.A.; Mayer, J.M. A Continuum of Proton-Coupled Electron Transfer Reactivity. *Acc. Chem. Res.* **2018**, *51*, 2391–2399. [[CrossRef](#)]
7. Agarwal, R.G.; Coste, S.C.; Groff, B.D.; Heuer, A.M.; Noh, H.; Parada, G.A.; Wise, C.F.; Nichols, E.M.; Warren, J.J.; Mayer, J.M. Free Energies of Proton-Coupled Electron Transfer Reagents and Their Applications. *Chem. Rev.* **2022**, *122*, 1–49. [[CrossRef](#)]
8. Warren, J.J.; Tronic, T.A.; Mayer, J.M. Thermochemistry of Proton-Coupled Electron Transfer Reagents and its Implications. *Chem. Rev.* **2010**, *110*, 6961–7001. [[CrossRef](#)]
9. Siewert, I. Proton-Coupled Electron Transfer Reactions Catalysed by 3d Metal Complexes. *Chem.—A Eur. J.* **2015**, *21*, 15078–15091. [[CrossRef](#)]
10. Cukier, R.I. Proton-Coupled Electron Transfer Reactions: Evaluation of Rate Constants. *J. Phys. Chem.* **1996**, *100*, 15428–15443. [[CrossRef](#)]
11. Huynh, M.T.; Mora, S.J.; Villalba, M.; Tejada-Ferrari, M.E.; Liddell, P.A.; Cherry, B.R.; Teillout, A.-L.; Machan, C.W.; Kubiak, C.P.; Gust, D.; et al. Concerted One-Electron Two-Proton Transfer Processes in Models Inspired by the Tyr-His Couple of Photosystem II. *ACS Cent. Sci.* **2017**, *3*, 372–380. [[CrossRef](#)]
12. Odella, E.; Mora, S.J.; Wadsworth, B.L.; Huynh, M.T.; Goings, J.J.; Liddell, P.A.; Groy, T.L.; Gervaldo, M.; Sereno, L.E.; Gust, D.; et al. Controlling Proton-Coupled Electron Transfer in Bioinspired Artificial Photosynthetic Relays. *J. Am. Chem. Soc.* **2018**, *140*, 15450–15460. [[CrossRef](#)]
13. Odella, E.; Wadsworth, B.L.; Mora, S.J.; Goings, J.J.; Huynh, M.T.; Gust, D.; Moore, T.A.; Moore, G.F.; Hammes-Schiffer, S.; Moore, A.L. Proton-Coupled Electron Transfer Drives Long-Range Proton Translocation in Bioinspired Systems. *J. Am. Chem. Soc.* **2019**, *141*, 14057–14061. [[CrossRef](#)]
14. Odella, E.; Mora, S.J.; Wadsworth, B.L.; Goings, J.J.; Gervaldo, M.A.; Sereno, L.E.; Groy, T.L.; Gust, D.; Moore, T.A.; Moore, G.F.; et al. Proton-coupled electron transfer across benzimidazole bridges in bioinspired proton wires. *Chem. Sci.* **2020**, *11*, 3820–3828. [[CrossRef](#)]

15. Goldsmith, Z.K.; Lam, Y.C.; Soudackov, A.V.; Hammes-Schiffer, S. Proton Discharge on a Gold Electrode from Triethylammonium in Acetonitrile: Theoretical Modeling of Potential-Dependent Kinetic Isotope Effects. *J. Am. Chem. Soc.* **2019**, *141*, 1084–1090. [[CrossRef](#)]
16. Warburton, R.E.; Hutchison, P.; Jackson, M.N.; Pegis, M.L.; Surendranath, Y.; Hammes-Schiffer, S. Interfacial Field-Driven Proton-Coupled Electron Transfer at Graphite-Conjugated Organic Acids. *J. Am. Chem. Soc.* **2020**, *142*, 20855–20864. [[CrossRef](#)]
17. Lam, Y.-C.; Soudackov, A.V.; Hammes-Schiffer, S. Theory of Electrochemical Proton-Coupled Electron Transfer in Diabatic Vibronic Representation: Application to Proton Discharge on Metal Electrodes in Alkaline Solution. *J. Phys. Chem. C* **2020**, *124*, 27309–27322. [[CrossRef](#)]
18. Sarkar, S.; Maitra, A.; Lake, W.R.; Warburton, R.E.; Hammes-Schiffer, S.; Dawlaty, J.M. Mechanistic Insights about Electrochemical Proton-Coupled Electron Transfer Derived from a Vibrational Probe. *J. Am. Chem. Soc.* **2021**, *143*, 8381–8390. [[CrossRef](#)]
19. Yadav, S.; Sharma, A.K.; Kumar, P. Nanoscale Self-Assembly for Therapeutic Delivery. *Front. Bioeng. Biotechnol.* **2020**, *8*, 127. [[CrossRef](#)]
20. Tan, M.; Tian, P.; Zhang, Q.; Zhu, G.; Liu, Y.; Cheng, M.; Shi, F. Self-sorting in macroscopic supramolecular self-assembly via additive effects of capillary and magnetic forces. *Nat. Commun.* **2022**, *13*, 5201. [[CrossRef](#)]
21. Li, K.; Hu, J.-M.; Qin, W.-M.; Guo, J.; Cai, Y.-P. Precise heteroatom doping determines aqueous solubility and self-assembly behaviors for polycyclic aromatic skeletons. *Commun. Chem.* **2022**, *5*, 104. [[CrossRef](#)]
22. Cui, Z.; Jin, G.-X. Construction of a molecular prime link by interlocking two trefoil knots. *Nat. Synth.* **2022**, *1*, 635–640. [[CrossRef](#)]
23. Woods, J.F.; Gallego, L.; Pfister, P.; Maaloum, M.; Vargas Jentzsch, A.; Rickhaus, M. Shape-assisted self-assembly. *Nat. Commun.* **2022**, *13*, 3681. [[CrossRef](#)] [[PubMed](#)]
24. Jiao, Y.; Qiu, Y.; Zhang, L.; Liu, W.-G.; Mao, H.; Chen, H.; Feng, Y.; Cai, K.; Shen, D.; Song, B.; et al. Electron-catalysed molecular recognition. *Nature* **2022**, *603*, 265–270. [[CrossRef](#)]
25. Whitesides, G.M.; Boncheva, M. Beyond molecules: Self-assembly of mesoscopic and macroscopic components. *Proc. Natl. Acad. Sci. USA* **2002**, *99*, 4769–4774. [[CrossRef](#)]
26. Gartner, F.M.; Graf, I.R.; Frey, E. The time complexity of self-assembly. *Proc. Natl. Acad. Sci. USA* **2022**, *119*, e2116373119. [[CrossRef](#)]
27. Deamer, D.; Singaram, S.; Rajamani, S.; Kompanichenko, V.; Guggenheim, S. Self-assembly processes in the prebiotic environment. *Philos. Trans. R. Soc. B Biol. Sci.* **2006**, *361*, 1809–1818. [[CrossRef](#)]
28. Wang, Z.; Gupta, R.K.; Luo, G.; Sun, D. Recent Progress in Inorganic Anions Templated Silver Nanoclusters: Synthesis, Structures and Properties. *Chem. Rec.* **2020**, *20*, 389–402. [[CrossRef](#)]
29. Gao, G.-G.; Cheng, P.-S.; Mak, T.C.W. Acid-Induced Surface Functionalization of Polyoxometalate by Enclosure in a Polyhedral Silver–Alkynyl Cage. *J. Am. Chem. Soc.* **2009**, *131*, 18257–18259. [[CrossRef](#)]
30. Shi, J.-Y.; Gupta, R.K.; Deng, Y.-K.; Sun, D.; Wang, Z. Recent Advances in the Asymmetrical Templatation Effect of Polyoxometalate in Silver Clusters. *Polyoxometalates* **2022**, *1*, 9140010. [[CrossRef](#)]
31. Fabre, B.; Falaise, C.; Cadot, E. Polyoxometalates-Functionalized Electrodes for (Photo)Electrocatalytic Applications: Recent Advances and Prospects. *ACS Catal.* **2022**, *12*, 12055–12091. [[CrossRef](#)]
32. Wu, Y.; Bi, L. Research Progress on Catalytic Water Splitting Based on Polyoxometalate/Semiconductor Composites. *Catalysts* **2021**, *11*, 524. [[CrossRef](#)]
33. Kuznetsov, A.E.; Geletii, Y.V.; Hill, C.L.; Morokuma, K.; Musaev, D.G. Dioxygen and Water Activation Processes on Multi-Ru-Substituted Polyoxometalates: Comparison with the “Blue-Dimer” Water Oxidation Catalyst. *J. Am. Chem. Soc.* **2009**, *131*, 6844–6854. [[CrossRef](#)]
34. Lauinger, S.M.; Piercy, B.D.; Li, W.; Yin, Q.; Collins-Wildman, D.L.; Glass, E.N.; Losego, M.D.; Wang, D.; Geletii, Y.V.; Hill, C.L. Stabilization of Polyoxometalate Water Oxidation Catalysts on Hematite by Atomic Layer Deposition. *ACS Appl. Mater. Interfaces* **2017**, *9*, 35048–35056. [[CrossRef](#)]
35. Anwar, N.; Sartorel, A.; Yaqub, M.; Wearan, K.; Laffir, F.; Armstrong, G.; Dickinson, C.; Bonchio, M.; McCormac, T. Surface Immobilization of a Tetra-Ruthenium Substituted Polyoxometalate Water Oxidation Catalyst Through the Employment of Conducting Polypyrrole and the Layer-by-Layer (LBL) Technique. *ACS Appl. Mater. Interfaces* **2014**, *6*, 8022–8031. [[CrossRef](#)]
36. Azmani, K.; Besora, M.; Soriano-López, J.; Landolsi, M.; Teillout, A.-L.; de Oliveira, P.; Mbomekallé, I.-M.; Poblet, J.M.; Galán-Mascarós, J.-R. Understanding polyoxometalates as water oxidation catalysts through iron vs. cobalt reactivity. *Chem. Sci.* **2021**, *12*, 8755–8766. [[CrossRef](#)]
37. Soriano-López, J.; Musaev, D.G.; Hill, C.L.; Galán-Mascarós, J.R.; Carbó, J.J.; Poblet, J.M. Tetracobalt-polyoxometalate catalysts for water oxidation: Key mechanistic details. *J. Catal.* **2017**, *350*, 56–63. [[CrossRef](#)]
38. Fertig, A.A.; Brennessel, W.W.; McKone, J.R.; Matson, E.M. Concerted Multiproton–Multielectron Transfer for the Reduction of O₂ to H₂O with a Polyoxovanadate Cluster. *J. Am. Chem. Soc.* **2021**, *143*, 15756–15768. [[CrossRef](#)]
39. Wang, X.-L.; Zhang, Y.; Chen, Y.-Z.; Wang, Y.; Wang, X. Two polymolybdate-directed Zn(II) complexes tuned by a new bis-pyridine-bis-amide ligand with a diphenylketone spacer for efficient ampere sensing and dye adsorption. *CrystEngComm* **2022**, *24*, 5289–5296. [[CrossRef](#)]
40. Huang, X.; Cui, Y.; Liu, G.; Wang, H.; Ren, J.; Zhang, Y.; Shen, G.; Lv, L.; Wang, H.-W.; Chen, Y.-F. Imidazole-Dependent Assembly of Copper Polymolybdate Frameworks for One-Pot Sulfide Oxidation and C–H Activation. *Energy Fuels* **2022**, *36*, 1665–1675. [[CrossRef](#)]

41. Liu, J.; Huang, M.; Hua, Z.; Dong, Y.; Feng, Z.; Sun, T.; Chen, C. Polyoxometalate-Based Metal Organic Frameworks: Recent Advances and Challenges. *ChemistrySelect* **2022**, *7*, e202200546. [[CrossRef](#)]
42. Talib, S.H.; Yu, X.; Lu, Z.; Ahmad, K.; Yang, T.; Xiao, H.; Li, J. A polyoxometalate cluster-based single-atom catalyst for NH₃ synthesis via an enzymatic mechanism. *J. Mater. Chem. A* **2022**, *10*, 6165–6177. [[CrossRef](#)]
43. Paul, A.; Das Adhikary, S.; Kapurwan, S.; Konar, S. En route to artificial photosynthesis: The role of polyoxometalate based photocatalysts. *J. Mater. Chem. A* **2022**, *10*, 13152–13169. [[CrossRef](#)]
44. Liu, S.; Cui, C.; Dai, Y.; Liu, G.; Qiao, S.; Tao, Y.; Zhang, Y.; Shen, G.; Li, Z.; Huang, X. Two silver-containing polyoxometalate-based inorganic-organic hybrids as heterogeneous bifunctional catalysts for construction of C–C bonds and decontamination of sulfur mustard simulant. *J. Solid State Chem.* **2022**, *316*, 123547. [[CrossRef](#)]
45. Silva, D.F.; Viana, A.M.; Santos-Vieira, I.; Balula, S.S.; Cunha-Silva, L. Ionic Liquid-Based Polyoxometalate Incorporated at ZIF-8: A Sustainable Catalyst to Combine Desulfurization and Denitrogenation Processes. *Molecules* **2022**, *27*, 1711. [[CrossRef](#)]
46. Veríssimo, M.I.S.; Evtuguin, D.V.; Gomes, M.T.S.R. Polyoxometalate Functionalized Sensors: A Review. *Front. Chem.* **2022**, *10*, 840657. [[CrossRef](#)]
47. Ren, W.; Li, B.; Li, S.; Li, G.; Gao, Z.; Chen, X.; Zang, H. Synthesis and Proton Conductivity of Two Molybdate Polymers Based on [Mo₈O₂₆]^{4−} Anions. *ChemistrySelect* **2022**, *7*, e202201337. [[CrossRef](#)]
48. Hsieh, T.C.; Shaikh, S.N.; Zubieta, J. Derivatized polyoxomolybdates. Synthesis and characterization of oxomolybdate clusters containing coordinatively bound diazenido units. Crystal and molecular structure of the octanuclear oxomolybdate (NH₄)₂(n-Bu₄N)₂[Mo₈O₂₀(NNPh)₆] and comparison to the structures of the parent oxomolybdate .alpha.-(n-Bu₄N)₄[Mo₈O₂₆] and the tetranuclear (diazenido)oxomolybdates (n-Bu₄N)₂[Mo₄O₁₀(OMe)₂(NNPh)₂] and (n-Bu₄N)₂[Mo₄O₈(OMe)₂(NNC₆H₄NO₂)₄]. *Inorg. Chem.* **1987**, *26*, 4079–4089.
49. Cindrić, M.; Vekseli, Z.; Kamenar, B. Polyoxomolybdates and polyoxomolybdovanadates—from structure to functions: Recent results. *Croat. Chem. Acta* **2009**, *82*, 345–362.
50. Chupina, A.V.; Shayapov, V.; Novikov, A.S.; Volchek, V.V.; Benassi, E.; Abramov, P.A.; Sokolov, M.N. [AgL]₂Mo₈O₂₆]^{n−} complexes: A combined experimental and theoretical study. *Dalton Trans.* **2020**, *49*, 1522–1530. [[CrossRef](#)]
51. Abramov, P.A.; Komarov, V.Y.; Pischur, D.A.; Sulyaeva, V.S.; Benassi, E.; Sokolov, M.N. Solvatomorphs of (Bu₄N)₂[(Ag(N₂-py))₂Mo₈O₂₆]: Structure, colouration and phase transition. *CrystEngComm* **2021**, *23*, 8527–8537. [[CrossRef](#)]
52. Komlyagina, V.I.; Romashev, N.F.; Kokovkin, V.V.; Gushchin, A.L.; Benassi, E.; Sokolov, M.N.; Abramov, P.A. Trapping of Ag⁺ into a Perfect Six-Coordinated Environment: Structural Analysis, Quantum Chemical Calculations and Electrochemistry. *Molecules* **2022**, *27*, 6961. [[CrossRef](#)]
53. Karoui, H.; Ritchie, C. Microwave-assisted synthesis of organically functionalized hexa-molybdovanadates. *New J. Chem.* **2018**, *42*, 25–28. [[CrossRef](#)]
54. Shuvaeva, O.V.; Zhdanov, A.A.; Romanova, T.E.; Abramov, P.A.; Sokolov, M.N. Hyphenated techniques in speciation analysis of polyoxometalates: Identification of individual [PMo_{12−x}V_xO₄₀]^{−3−x} (x = 1–3) in the reaction mixtures by high performance liquid chromatography and atomic emission spectrometry with inductively coupled. *Dalton Trans.* **2017**, *46*, 3541–3546. [[CrossRef](#)]
55. Mukhacheva, A.A.; Volchek, V.V.; Sheven, D.G.; Yanshole, V.V.; Kompankov, N.B.; Haouas, M.; Abramov, P.A.; Sokolov, M.N. Coordination capacity of Keggin anions as polytopic ligands: Case study of [VNb₁₂O₄₀]^{15−}. *Dalton Trans.* **2021**, *50*, 7078–7084. [[CrossRef](#)]
56. Mukhacheva, A.A.; Shmakova, A.A.; Volchek, V.V.; Romanova, T.E.; Benassi, E.; Gushchin, A.L.; Yanshole, V.; Sheven, D.G.; Kompankov, N.B.; Abramov, P.A.; et al. Reactions of [Ru(NO)Cl₅]^{2−} with pseudotrilaquary [XW₉O₃₃]^{9−} (X = As III, Sb III) anions. *Dalton Trans.* **2019**, *48*, 15989–15999. [[CrossRef](#)]
57. Kuznetsova, A.A.; Volchek, V.V.; Yanshole, V.V.; Fedorenko, A.D.; Kompankov, N.B.; Kokovkin, V.V.; Gushchin, A.L.; Abramov, P.A.; Sokolov, M.N. Coordination of Pt(IV) by [P₈W₄₈] Macrocylic Inorganic Cavitand: Structural, Solution, and Electrochemical Studies. *Inorg. Chem.* **2022**, *61*, 14560–14567. [[CrossRef](#)]
58. Chupina, A.V.; Mukhacheva, A.A.; Abramov, P.A.; Sokolov, M.N. Complexation and Isomerization of [β-Mo₈O₂₆]^{4−} in the Presence of Ag⁺ and DMF. *J. Struct. Chem.* **2020**, *61*, 299–308. [[CrossRef](#)]
59. Pantyukhina, V.S.; Volchek, V.V.; Komarov, V.Y.; Korolkov, I.V.; Kokovkin, V.V.; Kompankov, N.B.; Abramov, P.A.; Sokolov, M.N. Tubular polyoxoanion [(SeMo₆O₂₁)₂(C₂O₄)₃]^{10−} and its transformations. *New J. Chem.* **2021**, *45*, 6745–6752. [[CrossRef](#)]
60. Shmakova, A.A.; Akhmetova, M.M.; Volchek, V.V.; Romanova, T.E.; Korolkov, I.; Sheven, D.G.; Adonin, S.A.; Abramov, P.A.; Sokolov, M.N. A HPLC-ICP-AES technique for the screening of [XW₁₁NbO₄₀]^{n−} aqueous solutions. *New J. Chem.* **2018**, *42*, 7940–7948. [[CrossRef](#)]
61. Korpar-Čolig, B.; Cindrić, M.; Matković-Čalogović, D.; Vrdoljak, V.; Kamenar, B. Synthesis and characterization of some new acetato complexes of molybdenum(IV), (V) and (VI). *Polyhedron* **2002**, *21*, 147–153. [[CrossRef](#)]
62. Wang, S.; Mo, S.; Liu, Z.-G. Synthesis and characterization of a new octamolybdate (NH₄)₄[Mo₈O₂₄(C₃H₂O₂)₂]·4H₂O. *Russ. J. Inorg. Chem.* **2012**, *57*, 430–433. [[CrossRef](#)]
63. Brito, J.A.; Teruel, H.; Massou, S.; Gómez, M. ⁹⁵Mo NMR: A useful tool for structural studies in solution. *Magn. Reson. Chem.* **2009**, *47*, 573–577. [[CrossRef](#)] [[PubMed](#)]
64. Fedotov, M.A.; Maksimovskaya, R.I. NMR structural aspects of the chemistry of V, Mo, W polyoxometalates. *J. Struct. Chem.* **2006**, *47*, 952–978. [[CrossRef](#)]

-
65. Sheldrick, G.M. SHELXT—Integrated space-group and crystal-structure determination. *Acta Crystallogr. Sect. A Found. Adv.* **2015**, *71*, 3–8. [[CrossRef](#)]
 66. Sheldrick, G.M. Crystal structure refinement with SHELXL. *Acta Crystallogr. Sect. C Struct. Chem.* **2015**, *71*, 3–8. [[CrossRef](#)]
 67. Hübschle, C.B.; Sheldrick, G.M.; Dittrich, B. ShelXle: A Qt graphical user interface for SHELXL. *J. Appl. Crystallogr.* **2011**, *44*, 1281–1284. [[CrossRef](#)]